CrystEngComm

# Improving Pseudo-van der Waals Epitaxy of Self-Assembled InAs Nanowires on Graphene via MOCVD Parameter Space Mapping

| | |
|---|---|
| Journal: | *CrystEngComm* |
| Manuscript ID | CE-ART-09-2018-001666.R1 |
| Article Type: | Paper |
| Date Submitted by the Author: | 27-Oct-2018 |
| Complete List of Authors: | A Baboli, Mohadeseh; Rochester Institute of Technology, Microsystems Engineering; Rochester Institute of Technology, NanoPower Research Laboratories<br>Slocum, Michael; US Air Force Research Laboratory; Rochester Institute of Technology, NanoPower Research Laboratories<br>Kum, Hyun; Massachusetts Institute of Technology, Department of Mechanical Engineering; Rochester Institute of Technology, NanoPower Research Laboratories<br>Wilhelm, Thomas; Rochester Institute of Technology, Microsystems Engineering; Rochester Institute of Technology, NanoPower Research Laboratories<br>Polly, Stephen; Rochester Institute of Technology, NanoPower Research Laboratories<br>Hubbard, Seth M.; Rochester Institute of Technology, Microsystems Engineering; Rochester Institute of Technology, NanoPower Research Laboratories<br>Mohseni, Parsian; Rochester Institute of Technology, Microsystems Engineering; Rochester Institute of Technology, NanoPower Research Laboratories |
| | |

# Improving Pseudo-van der Waals Epitaxy of Self-Assembled InAs Nanowires on Graphene via MOCVD Parameter Space Mapping

**Mohadeseh A. Baboli[1,2], Michael A. Slocum[2,3], Hyun Kum[2,4], Thomas S. Wilhelm[1,2], Stephen J. Polly[2], Seth M. Hubbard[1,2], and Parsian K. Mohseni[1,2,*]**

[1]Microsystems Engineering, Rochester Institute of Technology, Rochester, NY 14623

[2]NanoPower Research Laboratories, Rochester Institute of Technology, Rochester, NY 14623

[3]Current Affiliation: Air Force Research Laboratory, Wright-Patterson Air Force Base, Dayton, OH 45433

[4]Current Affiliation: Department of Mechanical Engineering, Massachusetts Institute of Technology, Cambridge, MA 02139

*Author to whom correspondences should be addressed. E-mail: pkmohseni@rit.edu

**Abstract:** Heterogeneous self-assembly of III-V nanostructures on inert two-dimensional monolayer materials enables novel hybrid nanosystems with unique properties that can be exploited for low-cost and low-weight flexible optoelectronic and nanoelectronic device applications. Here, the pseudo-van der Waals epitaxy (vdWE) growth parameter space for heterogeneous integration of InAs nanowires (NWs) with continuous films of single layer graphene (SLG) via metalorganic chemical vapor deposition (MOCVD) is investigated. The length, diameter, and number density of NWs, as well as areal coverage of parasitic islands, are quantified as functions of key growth variables including growth temperature, V/III ratio, and total flow rate of metalorganic and hydride precursors. A compromise between self-assembly of high aspect ratio NWs comprising high number density arrays and simultaneous minimization of parasitic growth coverage is reached under a selected set of optimal growth conditions. Exploration of NW crystal structures formed under various growth conditions reveals that a characteristic polytypic and disordered lattice is invariant within the explored parameter space. A growth evolution study reveals a gradual reduction in both axial and radial growth rates within the explored timeframe for the optimal growth conditions, which is attributed to a supply-limited competitive growth regime. Two strategies are introduced for further growth optimization. Firstly, it is shown that the absence of a pre-growth *in situ* arsine surface treatment results in a reduction of parasitic island coverage by factor of ~0.62, while NW aspect ratio and number densities are simultaneously enhanced. Secondly, the use of a two-step flow-modulated growth procedure allows for realization of dense fields of high aspect ratio InAs NWs. As a result of the applied studies and optimization of the growth parameter space, we achieve the highest reported axial growth rate of 840 nm/min and NW number density of ~$8.3 \times 10^8$ $cm^{-2}$ for vdWE of high aspect ratio (>80) InAs NW arrays on graphitic surfaces. This work is intended to serve as a guide for vdWE of self-assembled III-V semiconductor NWs such as In-based ternary and quaternary alloys on functional two-dimensional monolayer materials, toward device applications in flexible optoelectronics and tandem-junction photovoltaics.

**Keywords:** InAs, nanowires, graphene, van der Waals epitaxy, metalorganic chemical vapor deposition, self-assembly, hybrid nanomaterials.

**Introduction**

Nanowire (NW) morphologies enable heteroepitaxy of largely dissimilar III-V compounds and provide a basis for design of high performance electronic [1,2] and photonic [3,4] devices that are otherwise inaccessible with planar structures. During conventional heteroepitaxy of planar geometries, strict constraints are imposed by the need to match lattice parameters, thermal expansion coefficients, and polar coherence between adjacent dissimilar materials. For example, tetragonal distortion suffered at the hetero-interface of two cubic compounds with largely incongruent lattice parameters results in the formation of misfit and threading dislocations after relaxation of the epilayer beyond a pseudomorphic critical thickness. Several approaches are available in thin film technology to overcome this fundamental limitation, such as growth of compositionally graded buffer layers [5–7], epitaxial lateral overgrowth [8–10], and aspect ratio trapping [11–13]. Although such techniques successfully achieve heterogeneous integration while preserving high crystalline quality, they also introduce additional pre-growth processing steps and/or require growth of passive layers, which add design complexity and increase fabrication costs. On the other hand, high aspect ratio structures with large surface area-to-volume ratios, such as NWs, offer the potential for elastic relaxation via strain accommodation along their free surfaces [14–18]. Consequently, without sacrificing the crystal quality or introducing cost-intensive fabrication steps, III-V semiconductor NWs can be directly integrated with various foreign substrates such as Ge [19], Si [20–22], glass [23], and even flexible carbon-nanotube composite films [24,25].

In recent years, the integration of III-V NWs with inert graphitic surfaces and functional two-dimensional (2-D) graphene nanosheets has also been explored [26–36]. Monolayer nanomaterials including single layer graphene (SLG), hexagonal boron nitride (h-BN), and transition metal dichalcogenides such as molybdenum disulfide ($MoS_2$) and tungsten diselenide ($WSe_2$) have shown promising performance in electronics [37], optoelectronics [38], photovoltaics [39,40], and photonics [41] applications. Through integration of III-V semiconductor NWs with 2-D nanomaterials, the unique properties of both nanostructure groups can be simultaneously exploited in the form of nano-hybrid materials system [26,27,36]. Additionally, transfer and re-distribution of interfacial charge states in such

integrated nanomaterials can enable unique optical and electronic properties that are distinct from those of the constituent materials [42,43]. Integration of this kind may be realized through the pseudo-van der Waals epitaxy (vdWE) approach, whereby an epi-layer is formed on an inert 2-D surface that provides no surface dangling bonds for covalent strain sharing [44]. In contrast to conventional epitaxy, vdWE does not require the extension of the substrate atomic order throughout the epilayer. In the case of pure vdWE, both components of a heteroepitaxial system possess strong intra-layer covalent bonds, while vdW interactions exist between adjacent planes. Alternatively, the pseudo-vdWE regime refers to the case where a 2-D material (e.g., graphene) and covalently-bonded bulk system (e.g., InAs) are directly interfaced, but separated by a vdW gap. Weak vdW forces between a monolayer substrate and III-V epilayer can accommodate nucleation and subsequent growth such that interfacial lattice distortion is mitigated and dislocation-free crystal assembly can take place.

Unlike semiconductor substrates with reactive dangling bonds, the growth surface of 2-D nanosheets offers limited positions for adatom adsorption and subsequent extension of the III-V lattice. In the case of graphene, the carbon honeycomb lattice allows three residence sites: (i) above a carbon site (T-site), (ii) above the bridge between a C-C bond (B-site), (iii) above the center of a hexagonal carbon lattice (H-site) [26]. As a result, and based on the lattice constant of a given III-V compound, there are limited possibilities for arrangement of atoms at the growth interface. Munshi et al. summarized possible atomic arrangement for binary III-V compounds with different lattice constants [26]. From a thermodynamic perspective, not all of these possible arrangements are achievable. This is due to the difference in binding energy between carbon atoms in the honeycomb lattice and atomic growth species that reside on T-, B-, or H-sites [45]. It has been shown that In adatoms may reside on energetically favorable H sites with bond energy of 1.29 eV [46]. This allows InAs to adopt its native lattice constant on SLG [47]. One notable limitation of the vdWE mode is that only a restricted set of materials systems (i.e., III-V lattices on 2-D monolayers) satisfy the above conditions that enable direct self-assembly of high aspect ratio nanostructures.

For the specific case of III-V NW vdWE on graphene or graphitic surfaces, various growth mechanisms have been employed to date. The self-catalyzed vapor-liquid-solid (VLS) approach via molecular beam

epitaxy (MBE) has been shown by Munshi and colleagues, whereby pre-deposited Ga droplets were used to form vertical GaAs NWs [26]. Similarly, Anyebe et al. have employed an In-seeded VLS approach to grow vertical InAs [31] and InAsSb [30] NWs by MBE. The Au-assisted VLS growth of vertical InGaAs NWs [35], as well as vertical and planar InAs, InP, GaAs, and GaP NWs [28], by metalorganic chemical vapor deposition (MOCVD) has also been shown. Importantly, in the case of MOCVD, vertical InAs and InGaAs NW vdWE can also proceed by a spontaneous self-assembly mechanism, which requires no pre-deposition of metallic seeding agents [27,29,35,36,47]. This has been attributed to the preferential formation of $(\bar{1}\bar{1}\bar{1})$-oriented InAs nuclei, enabled by the pseudo-coherent lattice alignment of cubic InAs along $\langle\bar{1}10\rangle$ relative to a ~6-fold multiple of the C-C bond length in SLG along $\langle1\bar{2}10\rangle$ [27,35]. Crystal growth then proceeds at an enhanced rate along the low-energy and vertically-oriented direction, thereby leading to the formation of free-standing NWs. Moreover, models presented by Hong et al. indicate that the vdW attraction can be further enhanced in such a nearly-commensurate lattice arrangement via In vacancy-mediated buckling of the basal InAs plane, which can cause an otherwise polar interface to become more flatly reconstructed [47].

The growth of InAs NWs by various epitaxial methods, as well as notable device applications that employ InAs NWs as active components, have been detailed in numerous review papers [48–50]. In contrast to the conventional seed-mediated or template-assisted growth modes, the simplicity of the MOCVD-based InAs NW vdWE approach, which requires no pre-growth surface pattering or pre-deposition of catalyst droplets, is highlighted as a key advantage. Nevertheless, precise tuning of growth conditions are needed and realization of optimal growth is non-trivial. The term optimal is used here to define the maximal aspect ratio of individual NWs comprising an array of maximal number density. Additionally, the term optimal is intended to describe a parameter space in which supplied growth species contribute predominantly to the formation of NW structures, such that parasitic growth of polycrystalline nano-islands is minimized. Several studies on vdWE of InAs NWs on SLG have been presented in the current literature. Comprehensive details regarding the self-assembly growth mechanism have been published in recent years [27,29,35,47]. Furthermore, NW-based photovoltaic solar cells and near-infrared photodetectors have been

demonstrated as device applications based on this nano-hybrid system, which was formed through vdWE [36,51]. Nonetheless, extensive evaluation of the growth window has only been carried out for the case of In-seeded NWs by MBE. Systematic mapping of the extended parameter space and a self-consistent correlation of growth conditions to NW morphology, NW number density, and areal coverage of parasitic islands during self-assembly of InAs NWs on SLG is needed for the MOCVD approach.

Here, a comprehensive exploration of the growth parameter space for self-assembly of InAs NWs on SLG by MOCVD vdWE is presented. In particular, the length, diameter, and number density of NWs, as well as the areal coverage of parasitic island growth is quantified as a function of MOCVD conditions including V/III ratio, growth temperature, and total flow rate of precursors. Growth trends are discussed in terms of underlying kinetic factors. By mapping a wide parameter space, growth conditions are simultaneously tuned for the formation of arrays with maximum NW aspect ratio, maximum NW number density, and minimum areal coverage of parasitic three-dimensional (3-D) nano-islands. The crystal structure of NWs grown under largely disparate conditions is analyzed to reveal a characteristically invariant polytypic NW lattice that is formed throughout the entire growth window. The evolution of NW morphologies over time is described with respect to axial and radial growth rates. The influence of a pre-growth arsine surface treatment is studied as an additional operational control that permits manipulation of NW densities. Finally, a two-step flow-modulated growth procedure is introduced for further optimization of NW aspect ratio and number density. Having a complete understanding of the MOCVD parameter space for seed-free and pattern-free growth of InAs NWs on SLG can be extended toward: (a) self-assembly of In-based ternary semiconductor compound NW structures such as $InAs_yP_{1-y}$ and $In_xAl_{1-x}As$ on 2-D surfaces [52], and (b) development of more accurate theoretical models for pseudo-vdWE based on verified experimental growth conditions. Such tuning of InAs NW growth conditions on 2-D nanomaterials is expected to inform the vdWE of a wide-ranging set of III-V semiconductor compounds and impact future device designs with applications in nanoelectronics, optoelectronics, and photovoltaics.

**Experimental Details**

Continuous CVD-grown monolayer graphene films transferred to 90 nm $SiO_2$-coated Si (100) substrates were commercially obtained from Graphene Supermarket Inc. and used as the growth surface in all vdWE experiments. The quality of as received graphene nanosheets was inspected by scanning electron microscopy (SEM), performed using a Hitachi S-4000 instrument. Low defect densities and monolayer thickness was confirmed via Raman spectroscopy using a multi-wavelength Jobin Yvon Horiba LabRAM HR Raman microscope. No graphene surface treatment or oxidation steps were carried out prior to loading in the MOCVD reactor, with the exception of a degreasing with a standard solvents. Growth of NWs was performed in an Aixtron 3×2" close coupled showerhead MOCVD reactor. Trimethyl-indium [TMIn, $(CH_3)_3In$] and arsine ($AsH_3$) were used as precursors for supply of In and As growth species, respectively. The growth parameter space investigated in the present work consisted of the following ranges: (i) growth temperature ($T_G$) was varied between 550 °C to 700 °C; (ii) V/III ratio was varied between 5 to 250 by changing $AsH_3$ flow rates at a constant TMIn flow rate; and (iii) TMIn flow rates ($\chi_{TMIn}$) were varied between 8 to 32 μmol/min. During all growths, hydrogen ($H_2$) was used as the carrier gas with total flow of 7 L/min, and the reactor pressure was kept constant at 100 mbar. Unless otherwise specified, all samples were heated to the desired $T_G$ under a constant $AsH_3$ flow before initiation of growth, which was marked by the introduction of TMIn flow. For all vdWE parameter space mapping trials, the total growth time ($t_G$) was kept constant at 300 seconds (shorter $t_G$ values are specified for the growth evolution study), and growth of InAs NWs was terminated by stopping TMIn flow while samples cooled under a constant $AsH_3$ flow. For comparison, additional trials were also performed wherein samples were cooled after growth termination under no $AsH_3$ flow.

As-grown NW samples were imaged for morphology and density measurements using a Hitachi S-4000 SEM and a TESCAN MIRA 3 SEM, equipped with energy dispersive x-ray spectrometry (EDXS) capabilities. The crystal structure of NWs grown under various conditions was observed using a FEI F20 high-resolution transmission electron microscopy (HR-TEM) system. Selected-area electron diffraction (SAED) patterns were obtained using the same instrument.

**Results and Discussions**

The main objective of this study is to investigate the vdWE parameter space and to correlate growth conditions to NW length, diameter, and density trends, as well as to changes in the areal coverage of parasitic islands. For systematic evaluation of growth parameter dependences, a series of growth trials are carried out wherein one of three individual variables (i.e., V/III ratio, $T_G$, and $\chi_{TMIn}$) are altered in the ranges specified above, while the other two variables are kept constant. In the following discussion, all trends presented for NW length, diameter, and aspect ratio consist of multiple data points, each of which quantifies the mean value measured from a set of 50 NWs per growth condition; error bars represent ±1 standard deviation from the mean. Values for NW density are measured from plan-view SEM images, and each data point represents the mean value based on 5 different sample locations consisting of >250 NWs; error bars represent the range of values measured at different locations. Values for areal coverage of parasitic islands are also measured from 5 different locations on the same sample based on plan-view SEM images, and each data point represents the mean percentage of total InAs-covered area minus the percentage of total area occupied by NWs; error bars indicate the range of measured values. Island and NW structures are distinguished based on size and contrast variances. Plan view images of as-grown samples were analyzed using an open-source image processing software, Fiji, and color segmentation plugin [53,54]. Contrast variances between high aspect ratio NWs, parasitic islands, and the background exposed graphene surf aces were exploited to determine the fraction of total imaged area covered by parasitic islands. The composition of as-grown InAs NWs and parasitic islands was confirmed via EDXS analysis (not shown here); additional elemental signatures that could be otherwise unintentionally introduced during MOCVD growth (e.g, Ga, Al, P, etc.) were not detected. We also note that Raman analysis of as-grown samples revealed that the quality of the SLG substrate was not detrimentally affected by the growth process, as equivalent D-band to G-band intensity ratios ($I_D/I_G$) were observed before and after growth.

***Mapping the V/III Ratio Parameter Space***

Firstly, V/III ratio dependences are considered for InAs NWs grown at constant $T_G$ = 650 °C and $\chi_{TMIn}$ = 16 μmol/min. The V/III ratio is varied between 5 and 250. Since NW growth is carried out here

under a high $T_G$ regime in comparison to InAs film growth, near-unity pyrolysis efficiency of TMIn is expected [55] such that metalorganic decomposition is not further increased in the presence of $AsH_3$ [56], and modification of the hydride supply alone will alter the true V/III ratio. Also, due the absence of pre-deposited metallic droplets, variances in local effective V/III ratio stemming from catalyst-mediated hydride decomposition are avoided [57] . Similar to the case of InAs NWs grown on Si by chemical beam epitaxy [58,59], V/III ratios above unity enable catalyst-free NW formation in the current study.

Shown in Figures 1(a)–(d) are 45° tilted-view SEM images of as-grown NW arrays at V/III ratio of 5, 25, 125 and 250. Figure 1(e) quantifies values for mean NW length (black square data points with solid trend line), mean NW diameter (white circle data points with dashed trend line), and mean NW aspect ratio (gray diamond data points with dotted trend line) as a function of V/III ratio. Consistent with Figure 1(a) and (b) SEM images, it is noted that raising V/III ratio from 5 to 25 results in over 2-fold increase in NW length. Below this range, insufficient $AsH_3$ supply results in sub-optimal NW axial growth rates. At V/III of 25, a maximum NW length of ~4.5 μm is observed within $t_G$ = 300 s. As the V/III ratio is further increased from 25 to 250, a gradual degradation in NW length is observed such that ~1 μm tall NWs are formed at V/III = 250. An opposite trend is found for NW diameter, which is minimized at ~50 nm in the V/III = 25 to 75 range, and increases monotonically beyond this range. Aspect ratio variances with V/III ratio follow the same trend as NW length, marked by a maximum aspect ratio of ~75 found at V/III = 25. In general, moderate V/III ratios in the range of 25 to 75 favor high aspect ratio NW growth.

While similar NW length and aspect ratio trends were observed within a comparable V/III ratio range in the case of In-seeded InAs NWs on graphite by MBE [31], NW diameters follow opposite variation tendencies. In the MBE study, increase in V/III ratio beyond ~50 brought about a nearly 2-fold decrease in NW diameters. This may be a result of catalyst droplet volume reduction via enhanced precipitation of In into the NW lattice under As-rich conditions [60]. In the current MOCVD study, the NW length and diameter trends may be understood simply in terms of surface mobility of In adatoms. Use of higher V/III ratios promotes vapor-solid growth on the NW sidewalls and thereby limits the supply of diffusive species

toward the NW top facet [61]. The result of both effects is the acceleration of radial growth at the expense of axial growth and, thus, the formation of thicker but shorter NWs.

The surface migration decay of growth species at elevated V/III ratios also results in reduced NW areal densities and greater coverage of 3-D islands. Figure 1(f) quantifies the number density of NWs per area (black square data points with solid trend line) and percentage of total surface area occupied by parasitic 3-D islands (white circle data points with dashed trend line). An inverse relationship between NW density and parasitic island coverage is noted with increasing V/III ratio, which can likely be attributed to a simple conservation of total supply of growth species. At V/III = 5, NW densities of ~$3.21 \times 10^8$ $cm^{-2}$ are calculated in comparison to densities of ~$4.75 \times 10^8$ $cm^{-2}$ at V/III = 25. Importantly, raising V/III ratio from 5 to 25 is accompanied with a dramatic reduction in areal coverage of islands (from ~46% to ~24%). Further increase in V/III ratio to 75 results in negligible change in NW density and moderate rise in island coverage (to ~26%), followed by a rapid decline in NW density and preferential formation of parasitic growth beyond V/III = 100. Use of V/III ratios above the optimal range of 25 to 75 results in the mitigation of In surface migration such that diffusive growth species are more effectively incorporated into parasitic islands of larger volume. While high V/III ratios favor island formation over NW growth, the lower number density NWs that are formed under such conditions experience enhanced radial growth rates over axial growth rates. Thus, elevated V/III ratio growth conditions are less conducive to fabrication of NW array-based devices, but may be exploited in applications where positioning of widely spaced NWs is required over extended 2-D nanosheet areas. To summarize, an extended V/III ratio space was investigated here (i.e. 5 – 250) and has resulted in growth of NWs with roughly twice the aspect ratio reported previously for seed-free InAs NWs grown on graphene by MOCVD [35], and roughly 7 times greater than the aspect ratio reported for In-seeded InAs NWs grown on graphitic substrates by MBE [31].

***Mapping the Growth Temperature Parameter Space***

Growth temperature dependences are considered for InAs NWs formed at constant V/III = 25 and $\chi_{TMIn}$ = 16 μmol/min. Under otherwise constant growth conditions, $T_G$ is varied between 550 °C and 700 °C in increments of 50 °C. Figures 2(a)–(d) show 45° tilted-view SEM images of as-grown samples formed in

this temperature range. As shown in Figure 2(a), NW self-assembly is entirely quenched at growth temperatures of 550 °C and below. In this low-$T_G$ range, a contiguous polycrystalline InAs film is formed through the merger of adjacent islands. Thus, lower growth temperatures may be exploited for pseudo-vdWE of III-V thin films on 2-D nanomaterials. At $T_G$ ~ 600 °C and above, vertically-oriented InAs NWs are self-assembled in large-area arrays with aspect ratios and number densities that are strongly dependent upon temperature. In Figure 2(e), measured mean values for NW length (black square data points with solid trend line), NW diameter (white circle data points with dashed trend line), and NW aspect ratio (gray diamond data points with dotted trend line) are plotted with respect to growth temperature. Similar to the observations by Anyebe et al. for InAs NWs grown on graphitic surfaces by MBE [31], a maximum NW aspect ratio is found at intermediate temperatures within the suitable $T_G$ range. In the current study, while mean values of NW length and diameter are observed to monotonically increase with $T_G$ in the 600 °C to 700 °C range, a relative enhancement of axial growth rate over radial growth rate at the intermediate of $T_G$ = 650 °C results in a maximum aspect ratio of ~75 after a 300 s growth period.

The above trends can be understood in terms of a balance between temperature-dependent surface mobility of group-III species and desorption of group-V species at the optimal growth temperature. As $T_G$ is raised from 600 °C to 650 °C, a corresponding increase in the thermally-activated surface mobility of group-III growth species enhances a supply of adatoms at the axial NW growth front, leading to a ~4-fold increase of mean NW length. Such a temperature change does not result in a significant variation of the mean NW diameter (i.e., nominal diameter increase between $T_G$ = 600 °C and $T_G$ = 650 °C is within measured statistical error). As $T_G$ is further raised from 650 °C to 700 °C, mean NW length is marginally influenced, quantified by an increase of ~30%. In contrast, radial growth is more dramatically impacted, resulting in over 3-fold enlargement of mean NW diameters. This can likely be attributed to thermal decomposition and enhanced desorption of group-V species at $T_G$ = 700 °C. A reduction in supply of diffusive growth species at the axial growth front can lead to accelerated rates of sidewall nucleation and, therefore, diameter expansion. A similar increase in radial NW growth at the expense of axial growth under elevated temperatures has been reported for various seed-free InAs NW systems [58,62]. Moreover, the

trends for NW length and diameter variation as a function temperature observed here are also representative of temperature-dependent growth trends reported for the diffusion-limited NW growth regime [63–68].

The number density and areal coverage of parasitic islands is also dramatically affected by growth temperature. Figure 2(f) plots the measured number density of NWs per area (black square data points with solid trend line) and surface area coverage percentage of parasitic 3-D islands (white circle data points with dashed trend line) with increasing $T_G$. As previously noted, low-temperature growth conditions favor the formation of low aspect ratio island structures leading to the deposition of contiguous films, quantified by nearly 100 % areal coverage of parasitic growth at $T_G$ = 550 °C. Above this temperature range, parasitic island coverage rapidly reduces, coincident with the initiation of NW growth in high number densities at 600 °C. The optimal $T_G$ range for high density NW array self-assembly is between 600 °C to 650 °C. However, as indicated in Figure 2(f), both the number density of NWs and areal coverage of parasitic island decrease with increasing temperature in the optimal $T_G$ range.

These observations may be explained based on the low adsorption energy of both In and As growth species on graphene, which itself possesses a low surface energy. While direct nucleation is enhanced on an As-terminated graphene surface in comparison to an unmodified and inert graphene surface [33], increasing $T_G$ results in preferential desorption of group-V species and, therefore, leads to a reduction in InAs nucleation rate. Consequently, the nucleation of both $(\bar{1}\bar{1}\bar{1})$-oriented InAs structures, which lead to NW formation, and otherwise oriented InAs nuclei, which contribute to parasitic growth, is quenched with increasing temperature. This is supported by the observation that the total areal coverage of InAs on the graphene surface, stemming from contributions from both NW and parasitic structures, rapidly decreases with rising $T_G$, as shown in the inset of Figure 2(f).

From a kinetic perspective, the notable distinction between growth at 600 °C and 650 °C is that, under a constant supply of group-III species (i.e., given near-unity decomposition efficiency of TMIn at all tested values of $T_G$ [55]), the diffusivity of adsorbed In atoms on both SLG and InAs surfaces is enhanced with temperature. Thus, surface migration toward the $(\bar{1}\bar{1}\bar{1})$-oriented NW top facet increases at 650 °C, leading to taller NWs that comprise an array of lower number density. With further increase of $T_G$ to 700

°C, the number density of NWs decays dramatically by ~96 % in comparison 600 °C. Above the optimal temperature range only few NWs form, likely due to prohibitively high group-V desorption. Parasitic structures with smooth surfaces are also observed at 700 °C, in contrast to the 3-D islands with well-defined crystalline facets found at lower temperatures; the former may result from preferential In clustering on the SLG surface. Given that the current parameter space is not tuned for self-catalyzed VLS growth, In droplets formed under the elevated temperatures fail to accommodate seed-mediated NW assembly. The small collection of NWs that are formed at 700 °C do so through a non-catalytic self-assembly mechanism, similar to those NWs formed at lower temperatures (as evidenced by the absence of In seeds at their tips via TEM inspection even under $AsH_3$-free post-growth cooling; not shown). Growth under such elevated temperatures may be exploited for applications that require more sparsely positioned vertical NWs on SLG. In summary, the effect of growth temperature on morphology and number density of InAs NWs, as well as areal coverage of parasitic island, for the case of seed-free InAs NWs on graphene via MOCVD has been investigated in a self-consistent approach. We highlight the highest reported axial growth rate of 1174 nm/min at an elevated temperature of 700 °C (in comparison to ~900 nm/min at an optimal temperature of 650 °C). The maximum growth rate found here is roughly 27 times faster than the reported growth rate of MBE-grown InAs NWs on graphitic substrates [31], and roughly 3.4 times faster than the growth rate of InAs NWs on SLG by MOCVD 35].

***Mapping the Total Molar Flow Rate Parameter Space***

The final growth parameter variation investigated here is the total molar flow rate of precursors. At constant $T_G$ = 650 °C, the total flow rate of precursors (i.e., $\chi_{Total} = \chi_{AsH3} + \chi_{TMIn}$), which can be considered as equivalent to a metric that tracks growth rate, was modified while maintaining a constant V/III ratio of 25. For simplicity, the results are reported and discussed with respect to the molar flow rate of TMIn, $\chi_{TMIn}$, as a single variable. However, it should be noted that the total flow of both metalorganics and hydrides was varied in sequential growth trials, while keeping V/III ratio constant.

Figures 3(a)–(d) show as-grown NW arrays formed under increasing TMIn flow rates, in the $\chi_{TMIn}$ = 8 to 32 μmol/min range. Figure 3(e) plots values of mean NW length (black square data points with solid

trend line), diameter (white circle data points with dashed trend line), and aspect ratio (gray diamond data points with dotted trend line) measured from samples grown at TMIn flow rates specified in panels (a)–(d). For the same set of growth trials, measured values of mean NW number density (black square data points with solid trend line) and surface area coverage percentage of parasitic 3-D islands (white circle data points with dashed trend line) are quantified in Figure 3(f). Under low-flow conditions of $\chi_{TMIn}$ = 8 μmol/min, NWs with mean lengths and diameters of ~1.4 μm and ~40 nm are formed, respectively, after a growth period of 300 s. Doubling the flow rate to $\chi_{TMIn}$ = 16 μmol/min induces a rapid enhancement of axial growth with only moderate increase in radial growth, such that NW lengths and diameters increase to ~4.5 μm and ~60 nm, respectively. The result is an approximate doubling of aspect ratio to a value of ~75 at 16 μmol/min. Under elevated precursor flow rate conditions, both NW length and diameter show little deviation from mean values observed at $\chi_{TMIn}$ = 16 μmol/min (i.e., within the measured error range), resulting in a saturation of aspect ratio.

This seemingly counterintuitive trend, whereby a continual increase of precursor supply fails to accommodate a corresponding increase in NW volume, can be understood with respect to a reduction of In atom diffusivity under higher $\chi_{TMIn}$ conditions and the role of parasitic islands as additional atomic sinks. As shown in Figure 3(f), NW number densities experience a monotonically decreasing trend while the areal coverage of parasitic islands continually grows with additional precursor supply. Nearly a four-fold reduction of NW number densities and over two-fold expansion of parasitic island coverage results from increasing TMIn flow rates from 8 to 32 μmol/min under a constant V/III ratio. As surface migration of In atoms is obstructed under higher flow rate conditions, preferential nucleation on 3-D islands causes rapid expansion of parasitic structures, while diffusion along NW sidewalls toward the low energy sink at the NW tips is quenched. Thus, excess supply of growth species under high $\chi_{TMIn}$ conditions contributes disproportionately to parasitic island growth over NW growth. The reduction in NW number density may stem from the coalescence of existing NW structures and laterally expanding parasitic structures during higher precursor supply conditions. The observed growth trends indicate that for simultaneous realization of NW arrays containing maximal number density and aspect ratio, a two-step flow-modulated growth

procedure involving a nucleation step at low-$\chi_{TMIn}$ and a subsequent axial extension step at higher-$\chi_{TMIn}$ may be utilized.

Based on the above growth trends, a suitable parameter set has been selected that represents a compromise between conditions that permit the formation of high aspect ratio NWs in high number density arrays and minimal surface coverage of parasitic 3-D islands. This parameter set, defined by *V/III* = 25, $T_G$ = 650 °C, and $\chi_{TMIn}$ = 16 μmol/min, is used as a basis or comparison point for additional experiments with the purpose of: (1) characterizing NW crystal structure; (2) tracking growth evolution; and (3) tuning NW number densities via pre-growth *in situ* surface treatment and use of a two-step flow-modulated growth procedure.

***Crystal Phase Analysis***

The influence of growth conditions on NW crystal structure is explored via HR-TEM imaging and SAED pattern analysis. Figure 4 shows representative TEM images of NWs obtained along the $\langle\bar{1}10\rangle_{\mathrm{ZB}}$ zone axis of the cubic phase from two different growths at $T_G$ = 650 °C. Images in panels (a)-(c) were obtained from a NW grown under a high V/III ratio of 250 and at the optimal precursor flow rate (i.e., $\chi_{TMIn}$ = 16 μmol/min). The black border in (a) highlights the approximate location of the image shown in (b), while the white border in (b) indicates the approximate location of the high-magnification and lattice-resolved micrograph displayed in (c). An SAED pattern recorded at the corresponding location is shown in (d). For comparison, images in panels (e)-(g) were collected from a NW grown at the optimal V/III ratio of 25, but under high precursor flow conditions (i.e., $\chi_{TMIn}$ = 32 μmol/min). The black and white boxes in (e) and (f) mark the locations of higher-magnification micrographs in subsequent panels, while (h) shows an SAED pattern recorded along the corresponding location.

Firstly, it is noted that NW morphologies shown in Figure 4 are consistent with dimensions described in the above discussion for the specified conditions. The NWs preferentially assemble along the $\langle\bar{1}\bar{1}\bar{1}\rangle_{\mathrm{ZB}}$ direction and are free of threading dislocations due to in-plane pseudo-coherency between InAs and SLG lattices [27,29,47]. Even in the absence of lattice-registry, strain relaxation via misfit dislocation

generation is not expected in the pseudo-vdWE regime, due to lack of hetero-interfacial covalency and strain sharing [35,44]. The NWs shown in Figure 4, as well as samples grown under all other conditions within the extended parameter space, exhibit a disordered crystal structure consisting of zinc-blende (ZB), wurtzite (WZ), and 4H polytype phases with a high density of stacking faults and rotational twin planes. Phase disorder and high planar defect density, visible as lateral striations in the micrographs, are also translated by prominent streaking along the $\langle \bar{1}\bar{1}\bar{1} \rangle_{ZB}$ axis in the SAED patterns. The crystal structures observed here are consistent with prior reports on vdWE-synthesized InAs and InGaAs on SLG [27,31,35,36,47]. The average interplanar spacing along the growth direction is measured to be ~3.517 Å. This measured value matches well with theoretical interplanar distance values of 3.516 Å and 3.520 Å for {111} $InAs_{ZB}$ and {0001} $InAs_{WZ}$, respectively [69]. Thus, as anticipated for the vdWE growth mode, the NW self-assembly process on SLG does not introduce additional lattice strain. Comparable interplanar spacing values (i.e., ~3.5 Å) along the growth direction have also been measured for self-catalyzed InAs NWs grown on graphite by solid-source MBE [31].

The representative NWs shown in Figure 4, which are either grown under moderate precursor flow and high V/III ratio [i.e., panels (a)-(d)] or moderate V/III ratio and high precursor flow conditions [i.e., panels (e)-(h)], exhibit no single phase WZ segments beyond 10 monolayers, regardless of position along the NW body. Extended ZB segments beyond 10 monolayers can be found, but such segments are not free of rotational twin planes. The same characteristic polytypic crystal structure is also observed for NWs grown under other conditions. The total density of planar defects (i.e., sum density of stacking faults and rotational twins) is measured to be ~500 $\mu m^{-1}$ in all NW samples investigated. Thus, crystal structure is observed to be independent of growth kinetics in the explored parameter space. Notably, the disordered structure extends throughout the tip region of all NWs inspected, regardless of whether or not samples are cooled from the growth temperature under $AsH_3$ flow. Neither a transition to a single crystal phase nor distinguishable variation in planar defect density is found along tip segments. This is in contrast to the commonly observed “cooling neck” effect in the case of In-catalyzed and Au-seeded InAs NWs, whereby

a ZB/WZ phase transition occurs near the catalyst/NW interface under reduced supersaturation conditions stemming from seed depletion in the absence of group-III supply at the end of growth [61,64,70].

The subject of phase mixing and polytypism between ZB and WZ structures in VLS-grown III-V semiconductor NWs has been extensively modelled on the basis of fundamental thermodynamics, and crystal phase control has been reliably demonstrated to be a function of growth kinetics [70–72]. The difference in bulk cohesive energy between ZB and WZ phases (i.e., 10.6 meV/octet pair for InAs [71]) is compensated in VLS-grown NW structures by a reduction in surface energy associated with WZ nucleus formation at a triple phase line [70]. This can enable crystal phase modulation by controlling the supersaturation of the metallic droplet (i.e., chemical potential difference between liquid and solid phases), which is realized by tuning of growth conditions for a given III-V material system [70–73]. Thus, by kinetically engineering the energy barrier to nucleation, the crystal structure of seed-based InAs NWs can be precisely transformed from ZB to WZ to 4H polytype during growth, as comprehensively demonstrated via both MBE and MOCVD [70,74–78]. In fact, it has been shown that even planar WZ InAs films can be formed through lateral extension from the base of WZ InAs NWs on ZB substrates [79]. However, for InAs NW self-assembly in the absence of a seed-mediated growth regime, control over phase purity is very challenging.

For the three most commonly employed seed-free InAs NW growth modes, which include selective-area epitaxy (SAE) of InAs NWs on various substrates [80–83], direct epitaxy (DE) of InAsP, InGaAs, and InAs NW on Si (111) substrates [21,84,85], and template-assisted epitaxy (TAS) of InAs NWs on Si (110) substrates [86], a disordered lattice consisting of a high density of planar defects is routinely found. While polytypism has been shown to be independent of Si dopant concentration [87–89], some notable alternative strategies have been applied during growth of catalyst-free In-based NWs to induce phase purity. Ji et al. have shown that the introduction of trimethyl-antimony during SAE growth results in the formation of purely ZB phase $InAs_{1-x}Sb_x$ NWs for $x = 9.4$ % [90]. Soo et al. realized catalyst-free growth of purely WZ InAs NWs on Si (111) through a nano-porous Ni masking layer by MOCVD [91]. While comparable $\chi_{TMIn}$ values were employed, the authors carried out growth at a lower V/III ratio (i.e., V/III =

2.9) and a prohibitively lower growth temperature (i.e., $T_G$ = 550 °C) than the current study. As described above, V/III < 25 renders low NW aspect ratio and number densities, while $T_G$ = 550 °C is not conducive to NW formation during vdWE of InAs on SLG. Lastly, Liu et al. have recently carried out comprehensive analysis of phase mixing during SAE of InAs on Si (111) by MOCVD [92]. The authors successfully realized growth of over 90% WZ phase, and concluded that high $T_G$, low absolute precursor flow rate, and low V/III ratio conditions are required to preferentially induce an InAs (111)B "unreconstructed" (1 × 1) surface, which favors hexagonal phase nucleation, as opposed to the (2 × 2) reconstructed surface, which favors ZB phase nucleation. While comparable V/III ratios and sufficiently high $T_G$ values were employed by Liu et al. as those in the current work, substantially lower precursor flow rates (i.e., $\chi_{TMIn}$ = 1 μmol/min) were required for phase purity. We conclude that, although modification of growth kinetics beyond the parameter window explored here may permit appreciable phase purity as realized by Soo et al. and Liu et al., our observations indicate that such conditions provide critical limitations with respect to template-free self-assembly of high aspect ratio InAs NW structures in arrays of high number density on SLG.

***Time Evolution Study***

Next, NW growth progression is tracked under the preferred parameter space defined by *V/III* = 25, $T_G$ = 650 °C, and $\chi_{TMIn}$ = 16 μmol/min. The time evolution of axial and radial growth is monitored over a series of seven runs toward the final growth duration of $t_G$ = 300 s. Figure 5(a)–(d) shows images from as-grown NW arrays that were formed under the above noted, constant growth conditions after growth periods of $t_G$ = 60 – 240 s, respectively (an array formed under the same conditions but after $t_G$ = 300 s is shown in Figure 1(b)). In Figure 5(e), the mean axial growth rates (black square data points and solid guide line) and mean radial growth rates (white circle data points and dashed guide line) are plotted for the 7 growth periods. While axial growth rates appear invariant within the measured error values in Figure 5(e), the inset plot showing NW length as a function of growth time clearly highlights a tendency toward reduced axial growth after $t_G$ = 180 s, as indicated by the solid portion of the gray fitted data line. Extrapolation of the same fitted curve toward the starting growth time, indicated by the dashed line segment, shows an absence of an extended incubation period and is contrary to what has been observed in the case of In-seeded InAs NW

growth by Grap et al. [60]. Hertenberger et al. emphasized a similarly absent nucleation phase prior to the onset selective-area MBE growth of InAs NWs in support of a seed-free growth mode [93]. It is noted that sidewall nucleation-mediated radial growth leads to continual expansion of the NW diameter over the entire growth period. However, as shown in Figure 5(e), the radial growth rate is observed to decline and saturate rapidly within this timeframe. The tendency toward a reduction in axial and radial growth rates is attributed to an increasing competition from additional surfaces for a limited material supply. As growth ensues, a constant supply of growth species is competitively distributed over an expanding collection of parasitic 3-D islands. Such a supply-limited competitive regime is exaggerated over time as island volumes grow and provide additional surfaces for nucleation, as visible in Figure 5(a)–(d). Thus, NW volume expansion declines over time. While growth rates are expected to saturate for longer growth times [93], the selected optimal conditions permit rapid axial growth rates of approximately 900 nm/min within the tested growth period. Compared to the reported growth rate of 43 nm/min for the case of In-seeded [31] and 340 nm/min for seed-free [35] InAs NWs on graphene, 11 nm/min for catalyst-free InAs on Si (111) [93], and 275 nm/min for InAs SAE on Si (111) [94], the optimized growth conditions in the current study enable maximum NW volume yield which holds promise for low-cost manufacturing of InAs NW arrays for applications in optoelectronics (i.e., photodetectors) and nanoelectronics (i.e., wrap-gated field–effect transistors).

***Growth Optimization for High NW Number Density Arrays***

Two additional optimization experiments are conducted with the intention of further reducing the areal coverage of parasitic islands and/or improving the NW number density under otherwise non-ideal conditions. In the first experiment, the purpose is to test the influence of a pre-growth *in situ* $AsH_3$ treatment on the formation of parasitic islands. Here, a low V/III ratio growth condition (i.e., $V/III = 5$, $T_G = 650$ °C, $\chi_{TMIn} = 16$ μmol/min) is selected as the starting point, which was shown earlier to produce relatively low NW number densities and high areal coverage percentage of parasitic islands. As demonstrated by Alaskar et al. [33], and noted earlier, the generation of an As-terminated graphene layer greatly enhances the surface energy and promotes further group-III adsorption. Thus, due to its chemically inert surface in the absence

of an As pre-layer, an enhancement of surface migration of growth species is expected, leading to fewer nucleation sites and a reduction of parasitic island coverage. Tilted-view SEM images of as-grown NW arrays formed with and without a 300 second pre-growth $AsH_3$ treatment at $T_G$ = 650 °C are shown in Figures 6(a) and (b), respectively. For growth without an $AsH_3$ pre-layer, the run was initiated at $T_G$ by simultaneously introducing TMIn and $AsH_3$ flows. In this case, a significant reduction (i.e., by a factor of ~0.62) in areal coverage of parasitic islands is observed. Correspondingly, a notable increase in NW number densities also occurs such that NWs are on average ~182% taller and ~128% larger in diameter than those NWs formed after pre-growth $AsH_3$ treatment. Therefore, the absence of an $AsH_3$ pre-layer not only results in the suppression of parasitic growth through a reduction (enhancement) of growth species adsorption (surface migration), but also leads to the formation of higher aspect ratio NWs in number densities under low V/III conditions that are comparable to those formed under optimal V/III conditions. The quantitative results from this growth are summarized in Table 1 and compared to results from samples grown with $AsH_3$ pre-layer under non-ideal and optimal V/III ratios of 5 and 25, respectively.

In the second optimization experiment, we return to the notion of a two-step flow-modulated growth procedure. As noted above, reduced precursor flow rates permit formation of high number density arrays of low aspect ratio NWs. Conversely, as precursor flow rates increase, NW aspect ratio is enhanced at the cost of number density and expansion of parasitic growth. In order to overcome this tradeoff, growth is first conducted at a low flow rate of $\chi_{TMIn}$ = 8 μmol/min for a period of 60 s as an initial "NW nucleation stage" so as to force the formation of high number density NW growth sites. Next, flow rates are increased such that $\chi_{TMIn}$ = 16 μmol/min for an additional 240 s growth period. Both growth steps are conducted at $T_G$ = 650 °C, and under constant V/III ratio (i.e., $AsH_3$ flow is also doubled during the second growth step).

A representative tilted-view SEM image of a sample formed under the two-step flow-modulated growth mode is shown in Figure 7, which can be compared to Figures 3(a) and (b) for the cases of fixed-flow growth at $\chi_{TMIn}$ = 8 μmol/min and $\chi_{TMIn}$ = 16 μmol/min, respectively. The corresponding growth metrics are summarized in Table 2 for these three trials. Through use of the flow-modulated growth mode, NW number densities are improved to comparable values that are realized under low flow rate conditions (i.e.,

> $8 \times 10^8$ cm$^{-2}$), without sacrificing NW aspect ratio or significantly influencing the axial growth rate (i.e., 840 nm/min). Thus, this optimized mode permits simultaneous realization of dense of NW arrays and formation of structures with aspect ratios greater than 80. However, under the two-step growth mode, the areal coverage of parasitic islands is observed to increase by more than a factor of two in comparison to alternative fixed-flow conditions. This can likely be attributed to rapid volume expansion during the second growth stage of a higher number density of parasitic islands that were initially formed during the first growth stage.

**Conclusions**

In summary, the exploration of an extended growth parameter space for self-assembly of InAs NWs on graphene by MOCVD has been presented. The dependences of NW length, diameter, and number density of as-grown arrays, as well as the areal coverage of unintentionally deposited parasitic islands, have been quantified as a function of critical epitaxy parameters including growth temperature, V/III ratio, and absolute flow rate of metalorganic and hydride precursors. A compromise between maximal NW aspect ratio, maximal NW number density, and minimal parasitic growth coverage is reached for the set of growth conditions defined by $T_G$ = 650 °C, $V/III$ = 25, and $\chi_{TMIn}$ = 16 μmol/min. While strategies for realization of the crystal phase purity during seed-free InAs NW growth have been discussed, it is noted that the NW crystal phase remains invariantly polytypic and comprised of disordered phases of ZB and WZ layers under all currently explored sets of growth conditions. Tracking the NW growth evolution under optimal conditions indicated that both axial and radial growth rates reduce and saturate over time, likely stemming from a growth regime wherein a constant precursor supply is competitively distributed amongst expanding NW and parasitic island volumes. It has been shown that growth results can be further optimized by two additional approaches. Elimination of a pre-growth *in situ* $AsH_3$ treatment causes reduction of growth species surface adsorption during the vdWE of InAs on SLG, which results in minimization of undesired parasitic growth. Moreover, use of a two-step flow-modulated growth mode has enabled further NW aspect ratio enhancement (i.e., to values > 80) as well as substantial increase in NW number densities (i.e. to values of ~$8.3 \times 10^8$ cm$^{-2}$). Gaining an understanding of the current parameter space provides a basis for the growth

of additional InAs-based ternary alloys through the incorporation of P and/or Al for extended bandgap engineering. This work is intended to serve as a guide for control over desired NW morphologies and number densities during vdWE growth of III-V NWs on inert substrates. While this materials system enables a series of nano-hybrid flexible nanoelectronics and optoelectronics device applications, it is also envisioned that III-V/SLG integrated nano-composites can be coupled to existing device architectures as supplementary components of hierarchical systems. Self-assembled arrays of In-based III-V NWs on SLG are also considered for use in tandem-junction solar cell designs as low bandgap sub-cells, such that SLG serves as a transparent and high-conductivity (i.e., n++) component of a tunnel junction when coupled to intermediate (e.g., Si) or high (e.g., GaAsP) bandgap sub-cells.

**Acknowledgements**

This material is based upon work supported by the National Science Foundation under Award No. 1665086. Also, this work made use of the Cornell Center for Materials Research Shared Facilities, which are supported through the NSF MRSEC program (DMR-1719875). M.A.B. and P.K.M. gratefully acknowledge John Grazul for TEM support. M.A.S. wishes to acknowledge support from the Intelligence Community Postdoctoral Research Fellowship program.

**ORCID iDs**

M A Baboli: https://orcid.org/0000-0001-8328-8713

M A Slocum: https://orcid.org/0000-0002-0434-8632

H Kum: https://orcid.org/0000-0002-8009-569X

T S Wilhelm: https://orcid.org/0000-0002-2689-0318

S M Hubbard: https://orcid.org/0000-0001-7661-4090

P K Mohseni: https://orcid.org/0000-0002-9377-7454

**References**


[1] B. Tian, X. Zheng, T. J. Kempa, Y. Fang, N. Yu, G. Yu, J. Huang and C. M. Lieber, *Nature*, 2007, **449**, 885.

[2] K. Tomioka, M. Yoshimura and T. Fukui, *Nature*, 2012, **488**, 189.

[3] M. E. Reimer, G. Bulgarini, N. Akopian, M. Hocevar, M. B. Bavinck, M. A. Verheijen, E. P. Bakkers, L. P. Kouwenhoven and V. Zwiller, *Nat. Commun.*, 2012, **3**, 737.

[4] R. Yan, D. Gargas and P. Yang, *Nat. Photon*, 2009, **3**, 569.

[5] R. Beanland, D. J. Dunstan and P. J. Goodhew, *Adv. Phys.*, 1996, **45**, 87–146.

[6] J. F. Geisz, J. M. Olson, M. J. Romero, C. S. Jiang and A. G. Norman, *Photovoltaic Energy Conversion, Conference Record of the 2006 IEEE 4th World Conference on*, IEEE, 2006, vol. 1, pp. 772–775.

[7] J. F. Geisz, D. J. Friedman, J. S. Ward, A. Duda, W. J. Olavarria, T. E. Moriarty, J. T. Kiehl, M. J. Romero, A. G. Norman and K. M. Jones, *Appl. Phys. Lett.*, 2008, **93**, 123505.

[8] R. W. McClelland, C. O. Bozler and J. C. C. Fan, *Appl. Phys. Lett.*, 1980, **37**, 560–562.

[9] Y. Ujiie and T. Nishinaga, *Jpn. J. Appl. Phys.*, 1989, **28**, L337.

[10] B.-Y. Tsaur, R. W. McClelland, J. C. Fan, R. P. Gale, J. P. Salerno, B. A. Vojak and C. O. Bozler, *Appl. Phys. Lett.*, 1982, **41**, 347–349.

[11] J.-S. Park, J. Bai, M. Curtin, B. Adekore, M. Carroll and A. Lochtefeld, *Appl. Phys. Lett.*, 2007, **90**, 052113.

[12] J. Bai, J.-S. Park, Z. Cheng, M. Curtin, B. Adekore, M. Carroll, A. Lochtefeld and M. Dudley, *Appl. Phys. Lett.*, 2007, **90**, 101902.

[13] J. Z. Li, J. Bai, J.-S. Park, B. Adekore, K. Fox, M. Carroll, A. Lochtefeld and Z. Shellenbarger, *Appl. Phys. Lett.*, 2007, **91**, 021114.

[14] P. K. Mohseni, C. Maunders, G. A. Botton and R. R. LaPierre, *Nanotechnology*, 2007, **18**, 445304.

[15] T. Mårtensson, C. P. T. Svensson, B. A. Wacaser, M. W. Larsson, W. Seifert, K. Deppert, A. Gustafsson, L. R. Wallenberg and L. Samuelson, *Nano Lett.*, 2004, **4**, 1987–1990.

[16] G. E. Cirlin, V. G. Dubrovskii, I. P. Soshnikov, N. V. Sibirev, Y. B. Samsonenko, A. D. Bouravleuv, J. C. Harmand and F. Glas, *Phys. Status Solidi RRL*, 2009, **3**, 112–114.

[17] F. Glas, *Phys. Rev. B*, 2006, **74**, 121302.

[18] E. Ertekin, P. A. Greaney, D. C. Chrzan and T. D. Sands, *J. App. Phys.*, 2005, **97**, 114325.

[19] E. P. A. M. Bakkers, J. A. van Dam, S. D. Franceschi, L. P. Kouwenhoven, M. Kaiser, M. Verheijen, H. Wondergem and P. van der Sluis, *Nat. Mater.*, 2004, **3**, 769–773.

[20] S. Plissard, G. Larrieu, X. Wallart and P. Caroff, *Nanotechnology*, 2011, **22**, 275602.

[21] J. C. Shin, A. Lee, P. K. Mohseni, D. Y. Kim, L. Yu, J. H. Kim, H. J. Kim, W. J. Choi, D. Wasserman and K. J. Choi, *ACS Nano*, 2013, **7**, 5463–5471.

[22] J. C. Shin, P. K. Mohseni, K. J. Yu, S. Tomasulo, K. H. Montgomery, M. L. Lee, J. A. Rogers and X. Li, *ACS Nano*, 2012, **6**, 11074–11079.

[23] V. Dhaka, T. Haggren, H. Jussila, H. Jiang, E. Kauppinen, T. Huhtio, M. Sopanen and H. Lipsanen, *Nano Lett.*, 2012, **12**, 1912–1918.

[24] P. K. Mohseni, G. Lawson, C. Couteau, G. Weihs, A. Adronov and R. R. LaPierre, *Nano Lett.*, 2008, **8**, 4075–4080.

[25] P. K. Mohseni, G. Lawson, A. Adronov and R. R. LaPierre, *IEEE J. Sel. Top. Quantum Electron.*, 2011, **17**, 1070–1077.

[26] A. M. Munshi, D. L. Dheeraj, V. T. Fauske, D.-C. Kim, A. T. van Helvoort, B.-O. Fimland and H. Weman, *Nano Lett.*, 2012, **12**, 4570–4576.

[27] Y. J. Hong, W. H. Lee, Y. Wu, R. S. Ruoff and T. Fukui, *Nano Lett.*, 2012, **12**, 1431–1436.

[28] J. Wallentin, D. Kriegner, J. Stangl and M. T. Borgström, *Nano Lett.*, 2014, **14**, 1707–1713.

[29] Y. J. Hong and T. Fukui, *ACS Nano*, 2011, **5**, 7576–7584.

[30] E. A. Anyebe, A. M. Sanchez, S. Hindmarsh, X. Chen, J. Shao, M. K. Rajpalke, T. D. Veal, B. J. Robinson, O. Kolosov and F. Anderson, *Nano Lett.*, 2015, **15**, 4348–4355.

[31] E. A. Anyebe, I. Sandall, Z. M. Jin, A. M. Sanchez, M. K. Rajpalke, T. D. Veal, Y. C. Cao, H. Li, R. Harvey and Q. D. Zhuang, *Sci. Rep.*, 2017, **7**, 46110.

[32] A. Mazid Munshi and H. Weman, *Phys. Status Solidi RRL*, 2013, **7**, 713–726.

[33] Y. Alaskar, S. Arafin, D. Wickramaratne, M. A. Zurbuchen, L. He, J. McKay, Q. Lin, M. S. Goorsky, R. K. Lake and K. L. Wang, *Adv. Funct. Mater.*, 2014, **24**, 6629–6638.

[34] V. Kumaresan, L. Largeau, A. Madouri, F. Glas, H. Zhang, F. Oehler, A. Cavanna, A. Babichev, L. Travers and N. Gogneau, *Nano Lett.*, 2016, **16**, 4895–4902.

[35] P. K. Mohseni, A. Behnam, J. D. Wood, C. D. English, J. W. Lyding, E. Pop and X. Li, *Nano Lett.*, 2013, **13**, 1153–1161.

[36] P. K. Mohseni, A. Behnam, J. D. Wood, X. Zhao, K. J. Yu, N. C. Wang, A. Rockett, J. A. Rogers, J. W. Lyding and E. Pop, *Adv. Mater.*, 2014, **26**, 3755–3760.

[37] G. Fiori, F. Bonaccorso, G. Iannaccone, T. Palacios, D. Neumaier, A. Seabaugh, S. K. Banerjee and L. Colombo, *Nat. Nanotechnol.*, 2014, **9**, 768.

[38] F. H. L. Koppens, T. Mueller, P. Avouris, A. C. Ferrari, M. S. Vitiello and M. Polini, *Nat. Nanotechnol.*, 2014, **9**, 780.

[39] A. Pospischil, M. M. Furchi and T. Mueller, *Nat. Nanotechnol.*, 2014, **9**, 257–261.

[40] M.-L. Tsai, M.-Y. Li, J. R. D. Retamal, K.-T. Lam, Y.-C. Lin, K. Suenaga, L.-J. Chen, G. Liang, L.-J. Li and -Hau He Jr, *Adv. Mater.*, 2017, **29**, 1701168

[41] F. Xia, H. Wang, D. Xiao, M. Dubey and A. Ramasubramaniam, *Nat. Photon.*, 2014, **8**, 899.

[42] F. Ning, D. Wang, Y.-X. Feng, L.-M. Tang, Y. Zhang and K.-Q. Chen, *J. Mater. Chem. C*, 2017, **5**, 9429–9438.

[43] C. Yelgel, G. P. Srivastava and R. H. Miwa, *J. Phys. Condens. Matter*, 2012, **24**, 485004.

[44] A. Koma, *J. Cryst. Growth*, 1999, **201**, 236–241.

[45] K. T. Chan, J. B. Neaton and M. L. Cohen, *Phys. Rev. B*, 2008, **77**, 235430.

[46] K. Nakada and A. Ishii, *Solid State Commun.*, 2011, **151**, 13–16.

[47] Y. J. Hong, J. W. Yang, W. H. Lee, R. S. Ruoff, K. S. Kim and T. Fukui, *Adv. Mater.*, 2013, **25**, 6847–6853.

[48] K. Tomioka, K. Ikejiri, T. Tanaka, J. Motohisa, S. Hara, K. Hiruma and T. Fukui, *J. Mater. Res.*, 2011, **26**, 2127–2141.

[49] Y. Zhang, J. Wu, M. Aagesen and H. Liu, *J. Phys. D*, 2015, **48**, 463001.

[50] V. G. Dubrovskii, G. E. Cirlin and V. M. Ustinov, *Semiconductors*, 2009, **43**, 1539.

[51] J. Miao, W. Hu, N. Guo, Z. Lu, X. Liu, L. Liao, P. Chen, T. Jiang, S. Wu and J. C. Ho, *Small*, 2015, **11**, 936–942.

[52] M. A. Baboli, M. A. Slocum, A. Giussani, S. M. Hubbard and P. K. Mohseni, *18th IEEE International Conference on Nanotechnology, Cork, Ireland,* 2018.

[53] J. Schindelin, I. Arganda-Carreras, E. Frise, V. Kaynig, M. Longair, T. Pietzsch, S. Preibisch, C. Rueden, S. Saalfeld and B. Schmid, *Nat. Methods*, 2012, **9**, 676.

[54] A. Griffa, T. Laroche, J. Artacho, J.-C. F. Sarria, D. Sage and N. Garin, *Development of Image-Analysis tools in the BioImaging and Optics platform (BIOp)*, ELMI, Davos, Switzerland, 2008.

[55] N. I. Buchan, C. A. Larsen and G. B. Stringfellow, *J. Cryst. Growth*, 1988, **92**, 591–604.

[56] C. A. Larsen, N. I. Buchan and G. B. Stringfellow, *Appl. Phys. Lett.*, 1988, **52**, 480–482.

[57] W. Sun, Y. Huang, Y. Guo, Z. M. Liao, Q. Gao, H. H. Tan, C. Jagadish, X. Z. Liao and J. Zou, *J. Mater. Chem. C*, 2015, **3**, 1745–1750.

[58] U. P. Gomes, D. Ercolani, N. V. Sibirev, M. Gemmi, V. G. Dubrovskii, F. Beltram and L. Sorba, *Nanotechnology*, 2015, **26**, 415604.

[59] U. P. Gomes, D. Ercolani, V. Zannier, J. David, M. Gemmi, F. Beltram and L. Sorba, *Nanotechnology*, 2016, **27**, 255601.

[60] T. Grap, T. Rieger, C. Blömers, T. Schäpers, D. Grützmacher and M. I. Lepsa, *Nanotechnology*, 2013, **24**, 335601.

[61] S. A. Dayeh, E. T. Yu and D. Wang, *Nano Lett.*, 2007, **7**, 2486–2490.

[62] G. Koblmüller, S. Hertenberger, K. Vizbaras, M. Bichler, F. Bao, J. P. Zhang and G. Abstreiter, *Nanotechnology*, 2010, **21**, 365602.

[63] P. Paiano, P. Prete, N. Lovergine and A. M. Mancini, *J. Appl. Phys.*, 2006, **100**, 094305.

[64] S. A. Fortuna, J. Wen, I. S. Chun and X. Li, *Nano Lett.*, 2008, **8**, 4421–4427.

[65] K. A. Dick, K. Deppert, L. S. Karlsson, L. R. Wallenberg, L. Samuelson and W. Seifert, *Adv. Funct. Mater.,* 2005, **15**, 1603–1610.

[66] S. N. Mohammad, *J. Vac. Sci. Techn. B*, 2010, **28**, 329–352.

[67] K. A. Dick, J. Bolinsson, M. E. Messing, S. Lehmann, J. Johansson and P. Caroff, *J. Vac. Sci. Techn. B*, 2011, **29**, 04D103.

[68] K. A. Dick, P. Caroff, J. Bolinsson, M. E. Messing, J. Johansson, K. Deppert, L. R. Wallenberg and L. Samuelson, *Semicon. Sci. Technol.*, 2010, **25**, 024009.

[69] H. Zheng, J. Wang, J. Y. Huang, J. Wang, Z. Zhang and S. X. Mao, *Nano Lett.*, 2013, **13**, 6023–6027.

[70] F. Glas, J.-C. Harmand and G. Patriarche, *Phys. Rev. Lett.*, 2007, **99**, 146101.

[71] V. G. Dubrovskii and N. V. Sibirev, *Phys. Rev. B*, 2008, **77**, 035414.

[72] V. G. Dubrovskii, N. V. Sibirev, J. C. Harmand and F. Glas, *Phys. Rev. B*, 2008, **78**, 235301.

[73] D. L. Dheeraj, G. Patriarche, H. Zhou, T. B. Hoang, A. F. Moses, S. Grønsberg, A. T. van Helvoort, B.-O. Fimland and H. Weman, *Nano Lett.*, 2008, **8**, 4459–4463.

[74] P. Caroff, K. A. Dick, J. Johansson, M. E. Messing, K. Deppert and L. Samuelson, *Nat. Nanotechnol.*, 2009, **4**, 50.

[75] K. A. Dick, C. Thelander, L. Samuelson and P. Caroff, *Nano Lett.*, 2010, **10**, 3494–3499.

[76] S. Lehmann, J. Wallentin, D. Jacobsson, K. Deppert and K. A. Dick, *Nano Lett.*, 2013, **13**, 4099–4105.

[77] M. Li, J. Wang, K. Li, Y. Xing and H. Q. Xu, *J. Cryst. Growth*, 2015, **430**, 87–92.

[78] Z. Zhang, Z. Lu, H. Xu, P. Chen, W. Lu and J. Zou, *Nano Res.*, 2014, **7**, 1640–1649.

[79] J. Bao, D. C. Bell, F. Capasso, N. Erdman, D. Wei, L. Fröberg, T. M\a artensson and L. Samuelson, *Adv. Mater.*, 2009, **21**, 3654–3658.

[80] K. Tomioka, J. Motohisa, S. Hara and T. Fukui, *Jpn. J. Appl. Phys.*, 2007, **46**, L1102.

[81] K. Tomioka, J. Motohisa, S. Hara and T. Fukui, *Nano Lett.*, 2008, **8**, 3475–3480.

[82] K. Tomioka, F. Izhizaka and T. Fukui, *Nano Lett.*, 2015, **15**, 7253–7257.

[83] H. Paetzelt, V. Gottschalch, J. Bauer, G. Benndorf and G. Wagner, *J. Cryst. Growth*, 2008, **310**, 5093–5097.

[84] M. T. Robson and R. R. LaPierre, *J. Cryst. Growth*, 2016, **436**, 1–11.

[85] J. C. Shin, K. H. Kim, K. J. Yu, H. Hu, L. Yin, C.-Z. Ning, J. A. Rogers, J.-M. Zuo and X. Li, *Nano Lett.*, 2011, **11**, 4831–4838.

[86] M. Borg, H. Schmid, K. E. Moselund, G. Signorello, L. Gignac, J. Bruley, C. Breslin, P. Das Kanungo, P. Werner and H. Riel, *Nano Lett.*, 2014, **14**, 1914–1920.

[87] J. Becker, M. O. Hill, M. Sonner, J. Treu, M. Döblinger, A. Hirler, H. Riedl, J. J. Finley, L. Lauhon and G. Koblmüller, *ACS Nano*, 2018, **12**, 1603–1610.

[88] E. Dimakis, M. Ramsteiner, C.-N. Huang, A. Trampert, A. Davydok, A. Biermanns, U. Pietsch, H. Riechert and L. Geelhaar, *Appl. Phys. Lett.*, 2013, **103**, 143121.

[89] S. Wirths, K. Weis, A. Winden, K. Sladek, C. Volk, S. Alagha, T. E. Weirich, M. von der Ahe, H. Hardtdegen and H. Lüth, *J. Appl. Phys.*, 2011, **110**, 053709.

[90] X. Ji, X. Yang, W. Du, H. Pan and T. Yang, *Nano Lett.*, 2016, **16**, 7580–7587.

[91] M. T. Soo, K. Zheng, Q. Gao, H. H. Tan, C. Jagadish and J. Zou, *Nano Lett.*, 2016, **16**, 4189–4193.

[92] Z. Liu, C. Merckling, R. Rooyackers, O. Richard, H. Bender, Y. Mols, M. Vila, J. Rubio-Zuazo, G. R. Castro and N. Collaert, *Phys. Rev. Mater.*, 2017, **1**, 074603.

[93] S. Hertenberger, D. Rudolph, M. Bichler, J. J. Finley, G. Abstreiter and G. Koblmüller, *J. Appl. Phys.*, 2010, **108**, 114316.

[94] M. T. Björk, H. Schmid, C. M. Breslin, L. Gignac and H. Riel, *J. Cryst Growth*, 2012, **344**, 31–37.

**Figure Captions**

**Figure 1.** V/III ratio dependence: 45° tilted-view SEM images of as-grown InAs NWs on SLG at V/III ratio of (a) 5, (b) 25, (c) 125, and (d) 250, under constant $T_G$ = 650 °C and $\chi_{TMIn}$ = 16 μmol/min. All scale bars represent 1 μm. (e) Measured values for NW length (black square data points with solid black line), diameter (white circle data point with dashed black line), and aspect ratio (grey diamond data points with dotted grey line), and (f) NW number density (black square data point with solid black line) and areal coverage of polycrystalline islands (white circle data points with dashed black line), plotted as functions of V/III ratio.

**Figure 2.** Temperature dependence: 45° tilted-view SEM images of as-grown InAs NWs on SLG at $T_G$ of (a) 550 °C, (b) 600 °C, (c) 650 °C, and (d) 700 °C, under constant V/III = 25, and $\chi_{TMIn}$ = 16 μmol/min. All scale bars represent 1 μm. Measured value for (e) NW height, diameter, and aspect ratio and (f) NW number density and parasitic island areal coverage are plotted as functions of $T_G$. Inset of (f) shows total areal coverage of both NWs and parasitic islands as a function of $T_G$.

**Figure 3.** Flow rate dependence: 45° tilted-view SEM images of as-grown InAs NWs on SLG at $\chi_{TMIn}$ of (a) 8 μmol/min, (b) 16 μmol/min, (c) 24 μmol/min, and (d) 32 μmol/min, under constant $T_G$ = 650 °C and V/III = 25. All scale bars represent 1 μm. Measured value for (e) NW height, diameter, and aspect ratio and (f) NW number density and parasitic island areal coverage are plotted as a function of $\chi_{TMIn}$.

**Figure 4.** TEM images obtained along the <110> zone axis (a-c, e-g) and corresponding SAD patterns (d, h) obtained from two different NWs both grown at $T_G$ = 650 °C. The NW captured in (a-d) was formed at high V/III ratio of 250, but at the optimal $\chi_{TMIn}$ = 16 μmol/min. The NW shown in (e-h) was formed at the optimal V/III ratio of 25, but at high $\chi_{TMIn}$ = 32 μmol/min. The highlighted regions in (a, b, e, f) are shown at higher magnification in subsequent panels.

**Figure 5.** Growth evolution of NWs under the selected optimal conditions of *V/III* = 25, $T_G$ = 650°C, and $\chi_{TMIn}$ = 16 μmol/min. (a-d) show 45° tilted-view images after growth durations of 60 s, 120 s, 180 s, and 240 s, respectively. All scale bars represent 1 μm. (e) NW axial growth rates (black square data points with solid black line) and NW radial growth rates (white circle data points with dashed black line) are plotted for various total growth times between 30 s and 300 s. The inset in (e) shows a plot of measured mean NW length versus growth time to demonstrate the growth rate saturation effect; a linear trend near the origin (i.e., dashed grey line for $t_s \leq 120$ s) is used to demonstrate the absence of a significant incubation phase prior to NW formation.

**Figure 6.** 45° tilted-view SEM images of as-grown InAs NWs formed under otherwise constant conditions, but (a) with and (b) without the use of a pre-growth $AsH_3$ surface treatment.

**Figure 7.** 45° tilted-view SEM image of high aspect ratio and high number density InAs NWs grown using a two-step flow-modulated sequence.

**Figure 1**

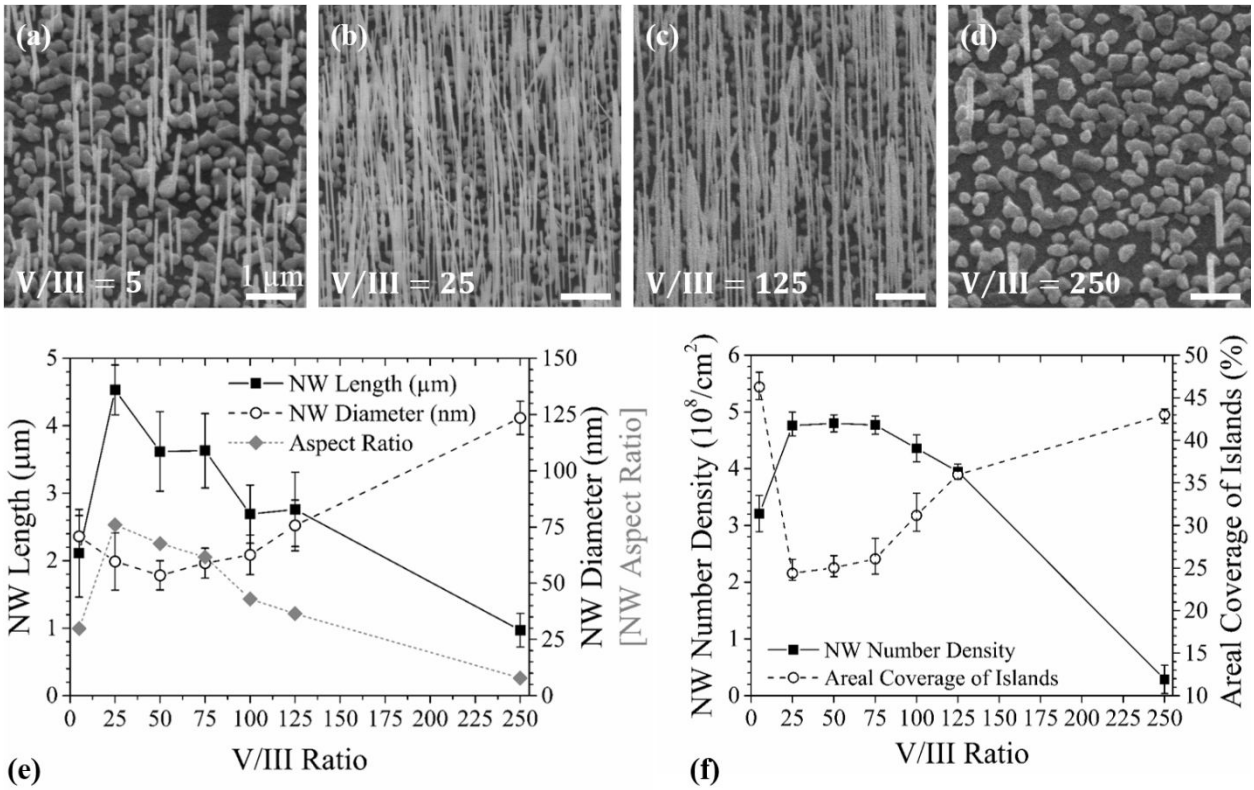
(a)
V/III = 5
1 μm
(b)
V/III = 25
(c)
V/III = 125
(d)
V/III = 250
NW Length (μm)
NW Diameter (nm)
Aspect Ratio
NW Length (μm)
NW Diameter (nm)
[NW Aspect Ratio]
V/III Ratio
(e)
NW Number Density
Areal Coverage of Islands
NW Number Density (10^8/cm^2)
Areal Coverage of Islands (%)
V/III Ratio
(f)

**Figure 2**

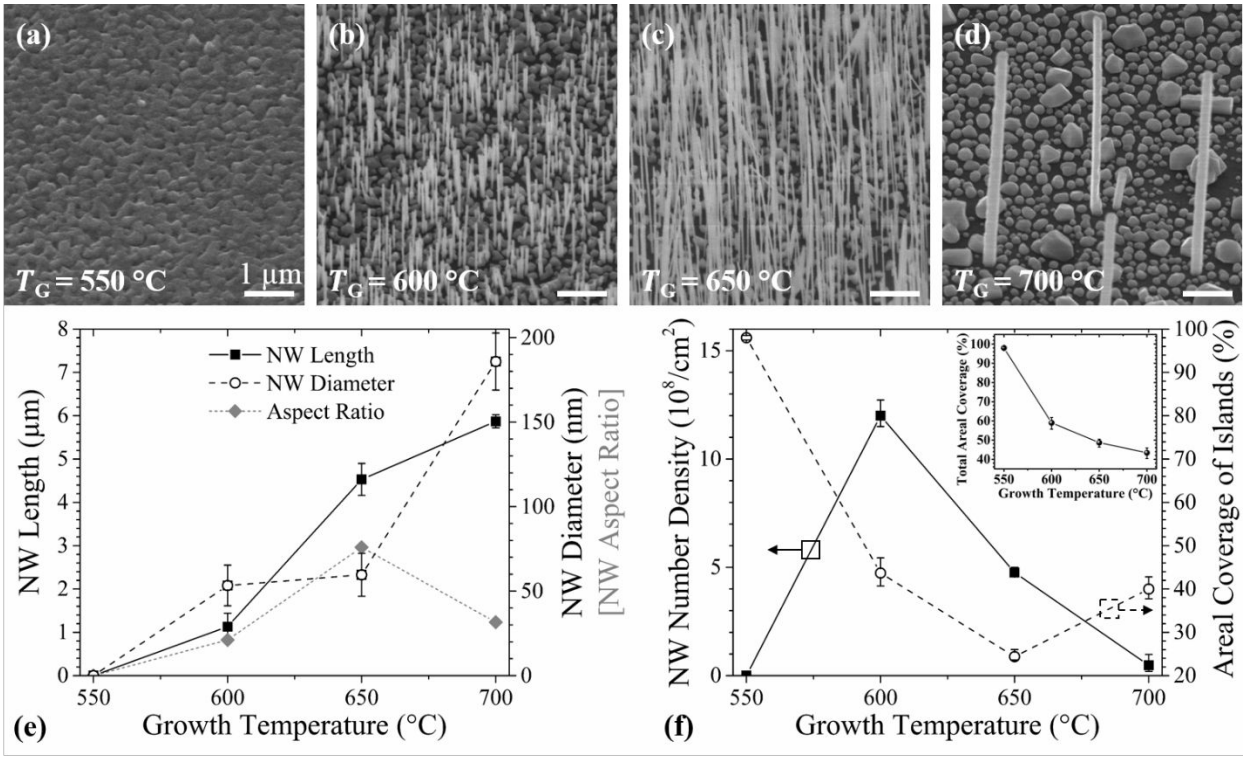
(a)
$T_G$ = 550 °C
1 μm
(b)
$T_G$ = 600 °C
(c)
$T_G$ = 650 °C
(d)
$T_G$ = 700 °C
NW Length
NW Diameter
Aspect Ratio
NW Length (μm)
NW Diameter (nm)
[NW Aspect Ratio]
Growth Temperature (°C)
(e)
NW Number Density ($10^8$/cm$^2$)
Areal Coverage of Islands (%)
Total Areal Coverage (%)
Growth Temperature (°C)
(f)

**Figure 3**

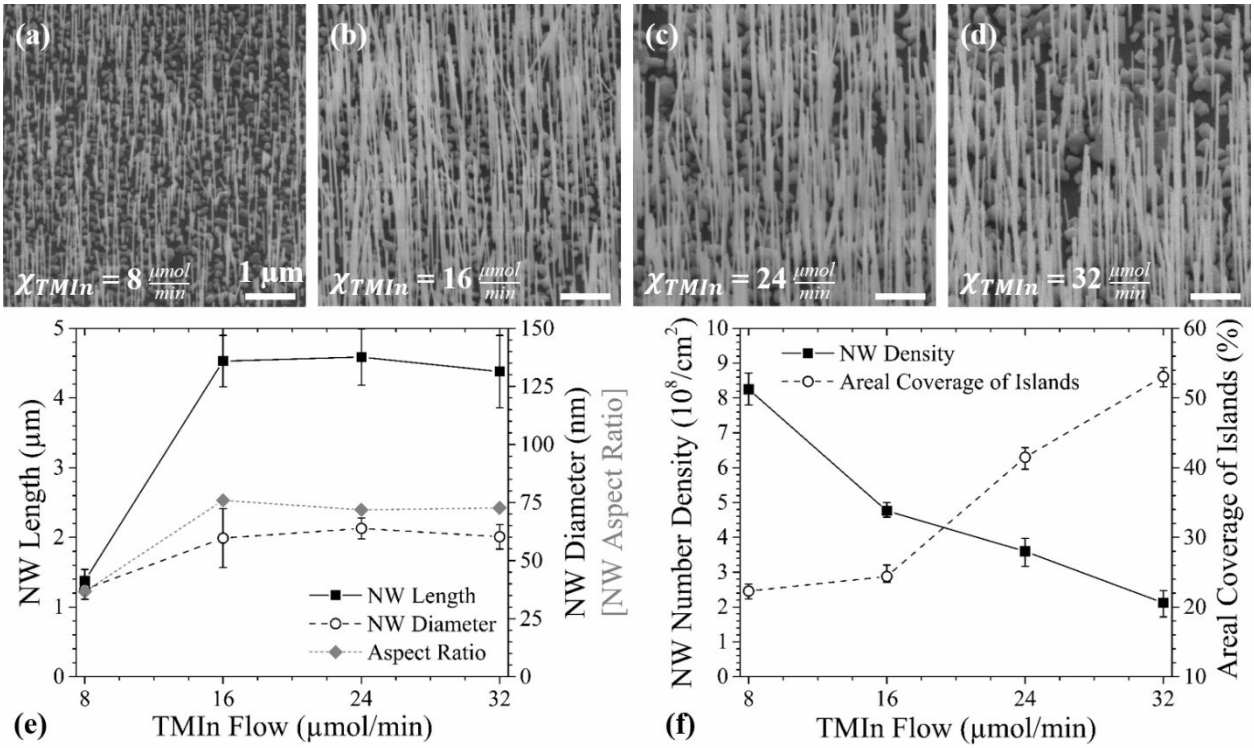
(a)
(b)
(c)
(d)
$\chi_{TMIn} = 8 \frac{\mu mol}{min}$
1 µm
$\chi_{TMIn} = 16 \frac{\mu mol}{min}$
$\chi_{TMIn} = 24 \frac{\mu mol}{min}$
$\chi_{TMIn} = 32 \frac{\mu mol}{min}$
NW Length (µm)
NW Diameter (nm)
[NW Aspect Ratio]
NW Length
NW Diameter
Aspect Ratio
TMIn Flow (µmol/min)
(e)
NW Number Density ($10^8$/cm$^2$)
Areal Coverage of Islands (%)
NW Density
Areal Coverage of Islands
TMIn Flow (µmol/min)
(f)

**Figure 4**

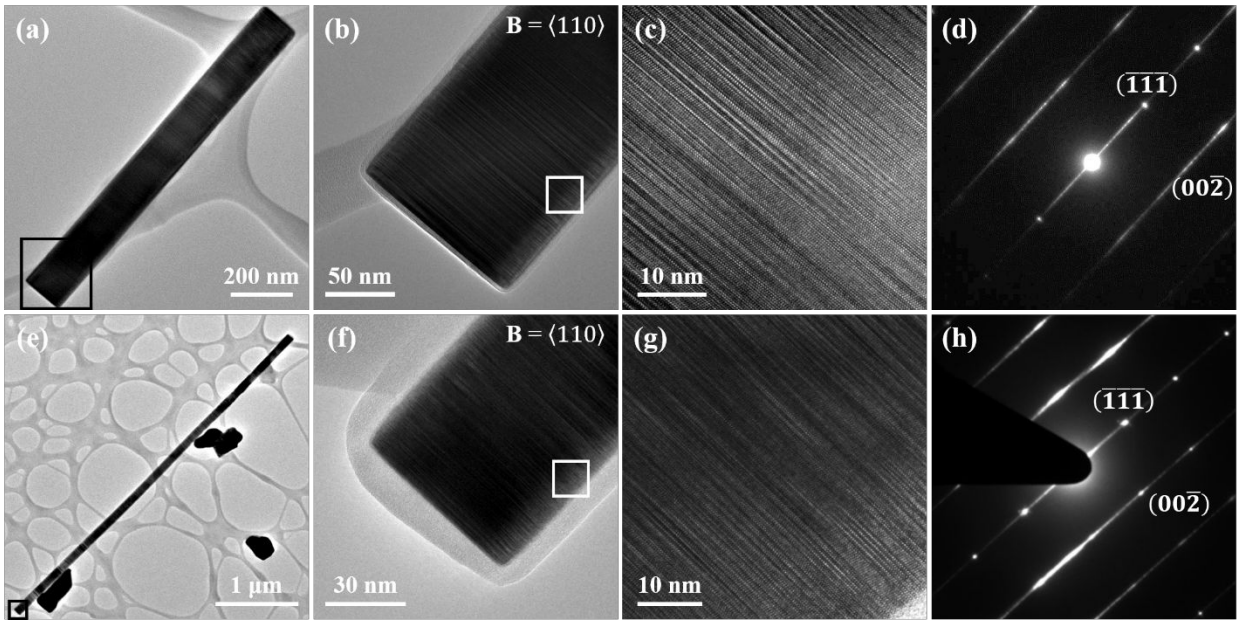
(a)
200 nm
(b)
B = ⟨110⟩
50 nm
(c)
10 nm
(d)
(111)
(00$\bar{2}$)
(e)
1 μm
(f)
B = ⟨110⟩
30 nm
(g)
10 nm
(h)
(111)
(00$\bar{2}$)

**Figure 5**

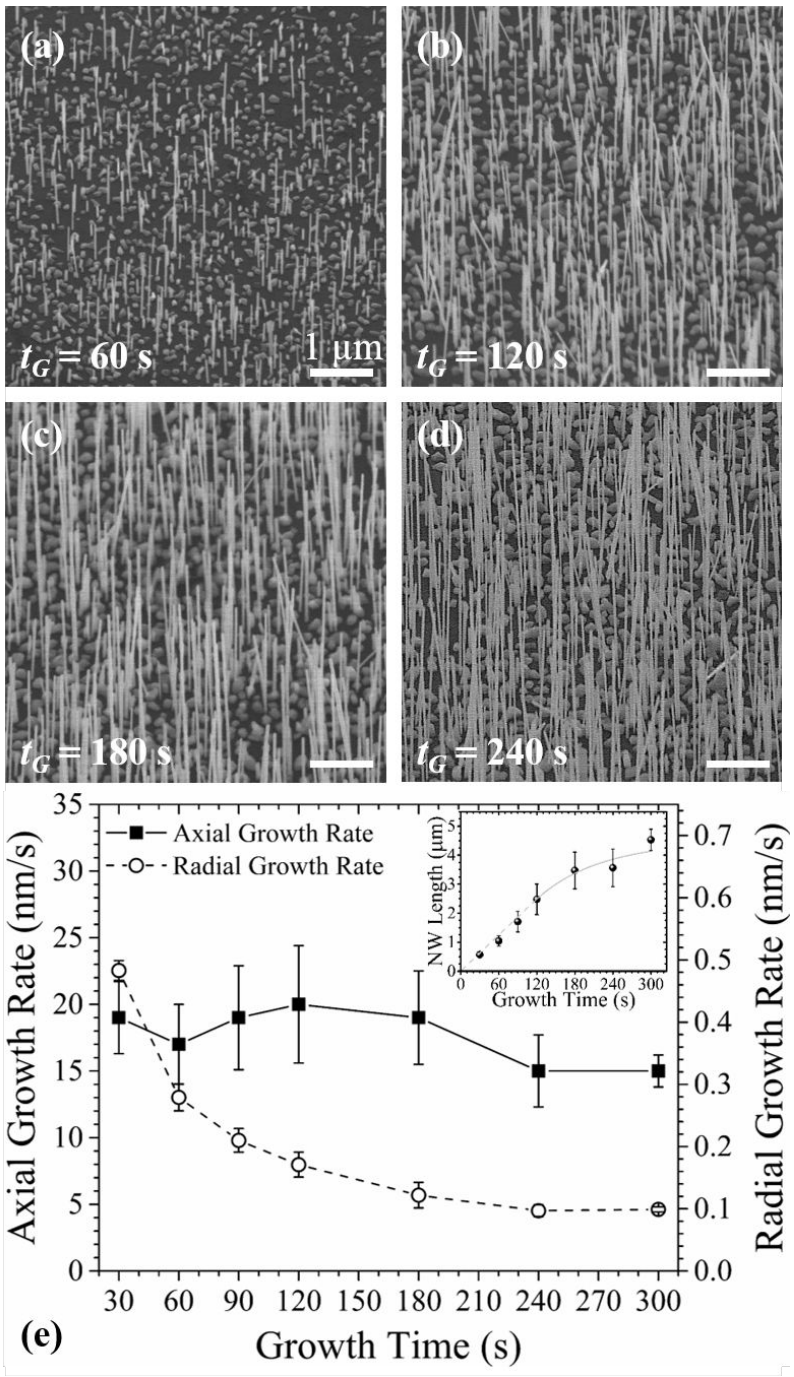
(a)
$t_G$ = 60 s
1 μm
(b)
$t_G$ = 120 s
(c)
$t_G$ = 180 s
(d)
$t_G$ = 240 s
Axial Growth Rate
Radial Growth Rate
NW Length (μm)
Growth Time (s)
Axial Growth Rate (nm/s)
Radial Growth Rate (nm/s)
Growth Time (s)
(e)

**Figure 6**

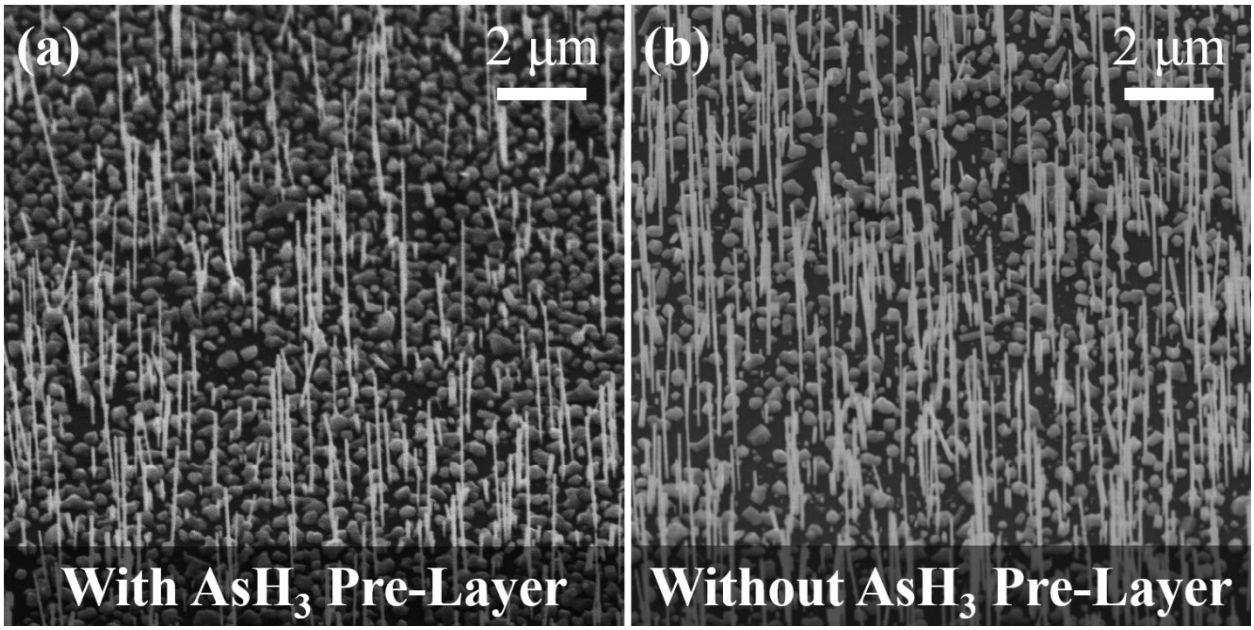

**Figure 7**

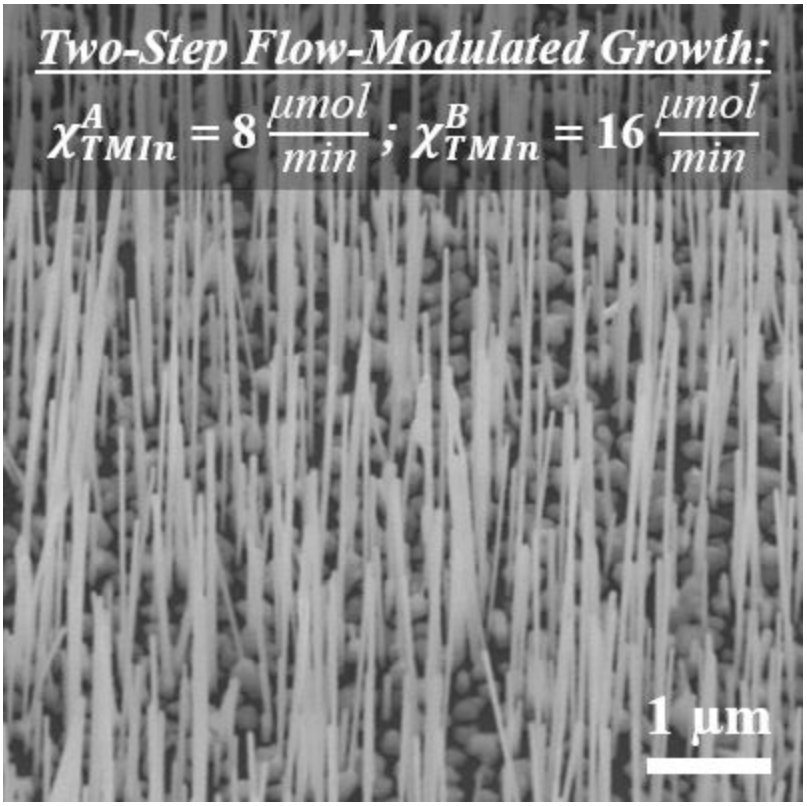
Two-Step Flow-Modulated Growth:
$\chi^{A}_{TMIn} = 8\,\frac{\mu mol}{min}$ ; $\chi^{B}_{TMIn} = 16\,\frac{\mu mol}{min}$
1 µm

*Table 1. Metrics for NW growths at V/III = 5 with and without $AsH_3$ pre-flow, compared to V/III = 25 with $AsH_3$ pre-flow.*

| **Growth Condition** | **Mean NW Length (µm)** | **Mean NW Diameter (nm)** | **NW Number Density ($cm^{-2}$)** | **Island Areal Coverage (%)** |
|---|---|---|---|---|
| *With $AsH_3$ Pre-Flow* *V/III* = 5 | 2.1 | 70.8 | $3.2 \times 10^8$ | 46.3 |
| *Without $AsH_3$ Pre-flow* *V/III* = 5 | 3.9 | 90.5 | $4.6 \times 10^8$ | 28.5 |
| *With $AsH_3$ Pre-Flow* *V/III* = 25 | 4.5 | 59.6 | $4.8 \times 10^8$ | 24.4 |

*Table 2. Metrics for NW growth under fixed-flow and two-step flow-modulated conditions.*

| **Growth Condition** | **Mean NW Length (μm)** | **Mean NW Diameter (nm)** | **NW Number Density ($cm^{-2}$)** | **Island Areal Coverage (%)** |
|---|---|---|---|---|
| *Fixed-Flow* $\chi_{TMIn}$ = 8 μmol/min for $t_G$ = *300 s* | 1.4 | 37.7 | $8.6 \times 10^8$ | 22.3 |
| *Fixed-Flow* $\chi_{TMIn}$ = 16 μmol/min for $t_G$ = *300 s* | 4.5 | 59.6 | $4.8 \times 10^8$ | 24.4 |
| *Two-Step Flow-Modulated* $\chi_{TMIn}$ = 8 μmol/min for $t_G$ = *60 s* $\chi_{TMIn}$ = 16 μmol/min for $t_G$ = *240 s* | 4.2 | 51.7 | $8.3 \times 10^8$ | 54.3 |